



HAL
open science

In situ carbon and oxygen isotopes measurements in carbonates by fiber coupled laser diode-induced calcination: a step towards field isotopic characterization.

Christophe Thomazo, Pierre Sansjofre, Olivier Musset, Théophile Cocquerez,
Stefan Lalonde

► To cite this version:

Christophe Thomazo, Pierre Sansjofre, Olivier Musset, Théophile Cocquerez, Stefan Lalonde. In situ carbon and oxygen isotopes measurements in carbonates by fiber coupled laser diode-induced calcination: a step towards field isotopic characterization.. *Chemical Geology*, 2021, 578, pp.120323. 10.1016/j.chemgeo.2021.120323 . hal-03328430

HAL Id: hal-03328430

<https://hal.science/hal-03328430>

Submitted on 24 May 2023

HAL is a multi-disciplinary open access archive for the deposit and dissemination of scientific research documents, whether they are published or not. The documents may come from teaching and research institutions in France or abroad, or from public or private research centers.

L'archive ouverte pluridisciplinaire **HAL**, est destinée au dépôt et à la diffusion de documents scientifiques de niveau recherche, publiés ou non, émanant des établissements d'enseignement et de recherche français ou étrangers, des laboratoires publics ou privés.



Distributed under a Creative Commons Attribution - NonCommercial 4.0 International License

In situ carbon and oxygen isotopes measurements in carbonates by fiber coupled laser diode-induced calcination: A step towards field isotopic characterization

Christophe Thomazo^{*1,2}, Pierre Sansjofre³, Olivier Musset⁴, Theophile Cocquerez¹, Stefan Lalonde⁵.

¹ Biogéosciences, CNRS UMR 6282, Université Bourgogne Franche-Comté, France

² Institut Universitaire de France

³ Muséum National d'Histoire Naturelle, Sorbonne Université, CNRS UMR 7590, IMPMC, 75005 Paris, France

⁴ Laboratoire Interdisciplinaire Carnot de Bourgogne, CNRS UMR 6303, Université de Bourgogne Franche-Comté, France

⁵ Laboratoire Géosciences Océan, Institut Universitaire Européen de la Mer, CNRS UMR 6538, France

*Corresponding author: christophe.thomazo@u-bourgogne.fr

Keywords (5): Carbon isotopes, oxygen isotopes, carbonates, laser, carbon cycle.

ABSTRACT:

Natural stable isotopes ratios ($\delta^{13}\text{C}_{\text{carb}}$ and $\delta^{18}\text{O}_{\text{carb}}$) of carbonates archived in the geological record are routinely used to reconstruct local and global paleo temperatures and the secular evolution of the biogeochemical carbon cycle. The state-of-the-art technique, employed since the mid 20th century, to measure these isotopic ratios starts with field sampling followed by several steps of physical and chemical laboratory preparation including: (i) microdrilling and/or sawing and crushing, (ii) CO_2 release by wet acid digestion, (iii) gas equilibration, purification and transfer, before (iv) gas phase IRMS measurements. While these steps are time and resource consuming, they provide accurate measurements of $\delta^{13}\text{C}_{\text{carb}}$, $\delta^{18}\text{O}_{\text{carb}}$ and carbonate contents. This study presents a new protocol involving a compact and modernized laser calcination system that decreases drastically the analyses time by reducing the number of preparations steps together with offering the possibility of performing spatially resolved analysis at the mm scale. This new method is based on the use of a fiber coupled laser diode device emitting 30 W in the near infrared at 880 nm. The energy provided by the laser source induces the decomposition of calcium

39 carbonate into lime and carbon dioxide. In this work, the CO₂ was collected in sample
40 tubes under a controlled atmosphere for offline analysis, however additional
41 developments should permit online analysis in the near future.

42 We analysed 9 different types of carbonate minerals encompassing a range of
43 isotopic compositions VPDB between +3.3 and -18.2‰ and between -1.7 and -
44 14.6‰ for $\delta^{13}\text{C}_{\text{carb}}$ and $\delta^{18}\text{O}_{\text{carb}}$, respectively. A comparison of isotopic results was
45 performed for carbonate zones analyzed both by classic methods (micro-drilling
46 followed by acid digestion) and laser calcination. This isotopic cross-calibration
47 exercise shows a direct positive co-variation between both methods with a correlation
48 coefficient of 0.99 and a regression slope of 1 within uncertainties for the $\delta^{13}\text{C}_{\text{carb}}$
49 values. The $\delta^{18}\text{O}_{\text{carb}}$ values also compared well with a correlation coefficient of 0.96,
50 suggesting a constant gas-solid phase isotopic equilibrium between carbon dioxide
51 and lime. The reproducibility of our laser calcination method performed on replicate
52 analyses of dolomite, siderite and malachite shows a 1σ standard deviation of 0.31
53 and 0.77 for $\delta^{13}\text{C}_{\text{carb}}$ and $\delta^{18}\text{O}_{\text{carb}}$, respectively. These reproducibilities are within the
54 observed isotopic natural inhomogeneity of samples (up to 1.3 and 0.57‰ for the
55 $\delta^{13}\text{C}_{\text{carb}}$ and $\delta^{18}\text{O}_{\text{carb}}$, respectively) as assessed by microdrilling and acid digestion.

56 Based on the suit of samples analyzed in this study, we demonstrate that (i)
57 fiber coupled laser diode calcination enables accurate and reproducible C and O
58 isotopic characterization of natural carbonates, (ii) physical effects during calcination
59 do not introduce any isotopic fractionation for C and is accompanied by a constant
60 isotopic offset for O over a range of isotopic compositions and mineral matrices.
61 These findings pave the way for a new range of possibilities for carbonate $\delta^{13}\text{C}$ and
62 $\delta^{18}\text{O}$ measurements directly in the field using rapid, portable, and easy to manipulate
63 laser preparation devices paired with CRDS/IRIS optical-mass spectrometers.

64

65

66 1. Introduction

67 Carbonates are among the most widely distributed minerals in the Earth's crust
68 and more than 3.5 billion years of Earth's history are chronicled in these rocks.
69 Carbonates play a major role in the global carbon cycle and in particular the long-
70 term sequestration of atmospheric CO₂ in sediments via silicate weathering followed
71 by carbonate precipitation (Berner et al., 1983). The latter played a critical role in
72 differentiating Earth's atmosphere from that of Mars, Venus or Mercury, and is
73 ultimately responsible for ensuring the habitability of our planet by keeping CO₂ in the
74 trace gas concentration range (Walker et al., 1981).

75 Understanding how carbonates are produced, from the formation of thin
76 sedimentary layers to the evolution of regional carbonate platforms, is a major
77 scientific challenge that has largely benefited from the study of their stable isotope
78 compositions. Up to now these measurements have been largely performed using
79 wet chemical preparation of the samples before Isotope Ratio Mass Spectrometer
80 (IRMS) analyses (McCrea, 1950) in a dedicated laboratory environment. In recent
81 years however, the development of a new generation of compact gas phase IRMS
82 instruments based on technologies such as Cavity Ring Down Spectroscopy (CRDS)
83 or Isotope Ratio Infrared Spectrometry (IRIS) now permit the analysis of atmospheric
84 CO₂ carbon and oxygen stable isotope ratios directly in the field (e.g. Garcia-Anton et
85 al., 2014; Rizzo et al., 2014; Fisher et al., 2016). A major barrier to the use of these
86 field-deployable instruments to measure the $\delta^{13}\text{C}$ and $\delta^{18}\text{O}$ of carbonates are the
87 traditional sample preparation steps: (i) crushing or microdrilling (with an optimal final
88 grain size lower than 140 μm), (ii) transfer of sample powder into vials, (iii) evacuation
89 of residual air by flushing with CO₂-free gas, and finally (iii) sample digestion using
90 several drops of orthophosphoric acid (H₃PO₄; McCrea, 1950). The reaction time is
91 generally between 15min and 48h, depending on carbonate mineralogy, before
92 isotopic measurements can be performed on the CO₂ evolved from the carbonate
93 sample. While this entire process is long and time consuming, it provides accurate
94 values of $\delta^{13}\text{C}_{\text{carb}}$, $\delta^{18}\text{O}_{\text{carb}}$ and carbonate content with typical internal reproducibility
95 of isotope ratios better than 0.1‰.

96 In situ laser extraction techniques were first developed in the 1990's to offer a
97 rapid, simple and high spatial resolution alternative to the conventional methods

98 describe above (Smalley et al., 1989; Smalley et al., 1992; Sharp, 1992; Sharp and
99 Cerling, 1996; Cerling and Sharp, 1996; Spötl and Matthey, 2006; McDermott, 2005;
100 Cosford et al., 2008; Hodge et al., 2008; Cosford et al., 2009; Cosford et al., 2010;
101 Baker et al., 2011; Baldini et al., 2015). For example, Sharp and colleagues (Sharp,
102 1992; Sharp and Cerling, 1996; Cerling and Sharp, 1996) proposed a laser
103 calcination technique using a 20W CO₂ laser (beam size >80µm) with a pulse
104 generator. The CO₂ is produced by calcination, following equation (1):



106
107
108 In this earlier set up, evolved CO₂ is frozen in a cold trap at liquid nitrogen
109 temperature, then transferred to an IRMS mass spectrometer. In Sharp and Cerling,
110 (1996), results were provided for 6 different types of carbonate minerals: calcite,
111 dolomite, magnesite, rhodochrosite, siderite, and smithsonite. They reported an
112 average reproducibility of 0.3‰ for δ¹⁸O_{carb} and 0.1‰ for δ¹³C_{carb} (1σ).

113 While these laser techniques clearly simplify sample preparation and permit
114 spatially resolved analysis, they still require cumbersome equipment, including a CO₂
115 laser (see supplementary information for size and weight characteristics), a liquid
116 nitrogen tank or a temperature regulated GC system, and an IRMS mass
117 spectrometer, which are all prohibitive to deployment outside of the laboratory.

118 The emergence of smaller, lighter and portable optical mass spectrometers based
119 on CRDS or IRIS, together with modern miniaturized laser sources, pave the way to
120 an entire new approach to carbon and oxygen isotopic measurements, including the
121 possibility of in situ isotopic mass spectrometry performed in the field. We propose in
122 this study a new technique and protocol for δ¹³C_{carb} and δ¹⁸O_{carb} analyses based on
123 laser calcination using a portable fiber coupled laser diode device that could be easily
124 paired to a CRDS/IRIS optical spectrometer.

125

126 **2. Conceptual frame work of laser calcination physics**

127 The reasoning of using a laser to trigger calcination reactions relies on local
128 material-light interactions as a spatially resolved source of heat. The incident laser
129 radiation is focused on a small area of the sample and the fraction of radiation not
130 reflected or scattered can then be absorbed by the material. Most of the absorbed

131 energy is then released quickly in the form of heat in a very small volume, which
132 leads to rapid and localized heating. This local heating allows the sample to reach
133 spontaneous calcination temperature and release CO₂. Complex models resolved in
134 space and time describing the laser calcination processes for rock cutting
135 applications can be found in the literature for different laser wavelengths and power
136 (Othman et al., 2019; Turchetta and Carrino., 2005; San-Roman-Alerigi et al., 2017;
137 San-Roman-Alerigi et al., 2018).

138 This work does not present detailed numerical modelling because it is beyond the
139 scope of this contribution. However, we consider in this study that the incident energy
140 of the laser beam is the sum of the reflected, diffused, absorbed and transmitted end
141 members. As the absorption coefficients of the materials are high in the visible or
142 near infrared, it can be considered that all of the transmitted radiation is absorbed
143 over a shallow depth. The absorbed energy E_{abs} can therefore be considered as the
144 product of the emissivity ε of the material multiplied by the incident laser energy E_{laser}
145 (equation 2). It follows that the energy can be express as the difference between
146 incident power P_{laser} minus reflected power $P_{reflected}$ multiplied by the duration of
147 exposure Δt

148

$$149 \quad E_{abs} = \varepsilon \cdot E_{laser} = (P_{laser} - P_{reflected}) \cdot \Delta t \quad (2)$$

150

151 Considering that all of the energy absorbed is transformed into heat, this
152 energy can be express as the sum of the energy of material heating (equation 3),
153 enthalpy of calcination, and heat losses (e.g. thermal conduction or ejection of
154 material or even radiation of the black body).

155

$$156 \quad E_{abs} = E_{Heat} + E_{calcination} + E_{thermal losses} \quad (3)$$

157

158 Considering this energy balance, it is necessary to reach temperatures of
159 around 900-950°C in order to trigger calcination reaction (Engler et al., 1989;
160 Turchetta and Carrino, 2005). Moreover, the heating energy depends not only on the
161 thermal and mechanical properties of the materials but also optical properties such
162 as emissivity and absorption coefficient. Similarly, the enthalpy of calcination
163 depends on the chemical structure (i.e. mineral lattice) and composition of the

164 sample (Othman et al., 2019). The balance between all these effects is complex, (but
165 excludes in our case the melting of lime which occurs at ca. 2570°C according to
166 Turchetta and Carrino (2005). The heat affected zone (i.e. HAZ) can also develop a
167 cooler zone in the middle which results from the ejection of produced lime powder by
168 CO₂. This can further complicate the energetic balance. To trigger calcination, it is
169 therefore necessary to provide sufficient energy per unit of volume and time to reach
170 the calcination temperature (100-200kJ / mol) and provide an energy equivalent to
171 the enthalpy of calcination (50-100kJ / mol). The calcination thresholds and the
172 production of CO₂ as a function of laser energy will therefore be very dependent on
173 the material exposed.

174 In the following sections, the laser intensity I at the focal point is also
175 considered in addition to the laser energy or laser power (see supplementary
176 information for detailed information on laser optical characteristics and a comparison
177 of fiber coupled laser diode modules with CO₂ lasers). For this, the radius of the laser
178 spot ω_0 is considered on the sample at the focal point of a lens of focal length f , for a
179 laser source with a Gaussian spatial profile quality of beam M^2 , of wavelength λ and
180 beam diameter at the entry of the lens W_{in} (equation 4):

$$\omega_0 = \frac{4 \cdot M^2 \cdot \lambda \cdot f}{\pi \cdot W_{in}} \quad (4)$$

184 The intensity I can then be written as the ratio between the incident power of the
185 laser divided by the surface at the focal point (equation 5):

$$I = \frac{P_{laser}}{\pi \omega_0^2} \quad (5)$$

189 3. Material and methods

190 3.1 Sample descriptions

191 Nine different types of carbonate minerals archetypal of Earth's chemical and
192 isotopic diversity have been selected for this study and are listed in Table 1. The
193 samples (see supplementary information for pictures) have been chosen in order to
194 reflect a large range in chemical composition, type of matrix, grain size and colour.
195 Preliminary tests demonstrated that transparent varieties of carbonate, such as

196 Iceland spar, showed poor calcination characteristics due to their very low absorption
197 coefficient in the near-IR range, and were discarded from the study.

198

	Sample	Description	Formula	Origin	ID number
1	Calcite 1	Speleothem	CaCO ₃	DMC	nr
2	Calcite 2	Ferroancalcite	CaCO ₃	DMC	nr
3	Dolomite 1	Micrite	CaMg(CO ₃) ₂	DMC	76-5
4	Dolomite 2	Saccharoid	CaMg(CO ₃) ₂	Saxony (DMC)	912
5	Siderite	Macrocrystal	FeCO ₃	DMC	nr
6	Malachite	Macrocrystal	Cu ₂ CO ₃ (OH) ₂	Siberia (DMC)	472
7	Rhodocrosite	Macrocrystal	MnCO ₃	Rothenberg Mine (DMC)	985
8	SDV	Dolomicrite	CaMg(CO ₃) ₂	Noonday Fm. (USA)	nr

199

200

201

202

203

204

Table 1: Carbonate mineral list and sample characteristics. Sample: name of the sample. Description: main lithological aspect. Formula: chemical formula of the considered carbonate. Origin: Dijon Museum Collection (DMC). Number: inventory number. Nr: Non-referenced material. SDV is a Neoproterozoic stromatolitic cap dolostone (Mg/Ca ratio of 0.52) deposited around 635 Ma in the aftermath of the Marinoan Snowball Earth.

205 3.2 Carbon and oxygen isotope analyses

206 All stable isotope analyses were performed at the Biogeosciences Laboratory,
207 Université Bourgogne Franche-Comté, Dijon, France.

208 Samples were analysed twice using state of the art micro-drilling and wet
209 chemistry preparation before IRMS analyses (McCrea, 1950) and using the laser
210 calcination device described in detail below.

211 Samples were first micro-drilled several times (between 10 and 15) depending on
212 the size of the samples in order to estimate spatial isotopic homogeneity. Then, 50 to
213 100 µg of each micro-drilled powders were loaded in glass vials and reacted with a
214 102% H₃PO₄ solution at 70°C for 20 minutes. Carbon and oxygen isotopic
215 compositions were measured on a ThermoScientific™ Delta V Plus™ IRMS coupled
216 with a Kiel VI carbonate preparation device. All isotope values are reported in the
217 standard δ-notation (in ‰) relative to the international standard VPDB (Vienna Pee
218 Dee Belemnite) using a δ¹³C value of +1.95‰, and a δ¹⁸O value of -2.20‰ for the
219 international standard NBS19 (Coplen et al., 2006) analyzed in the same sessions.
220 External reproducibility was assessed by replicate analyses of both NBS19 and in-
221 house laboratory calcite and dolomite standards and is better than ±0.07‰ (2σ).
222 Specific oxygen isotopes fractionation factor between H₃PO₄ and evolved CO₂ due to

223 cationic solid substitution (Rosenbaum and Sheppard, 1986; Böttcher, 1996) are not
224 considered in this study.

225 Samples were then loaded in the laser device (see section 3.3), and the evolved
226 CO₂ produced after laser calcination was collected in glass tubes and connected to
227 the dual inlet sample port of the ThermoScientific™ Delta V Plus™ IRMS. Samples
228 were then analysed against the Dijon Biogeosciences Laboratory in-house reference
229 gas. A mass to charge ratios (m/z) scan of these samples was also performed
230 following the isotopic analyses.

231 Before and after each “laser analytical session”, the in-house reference gas was
232 verified for its calibration vs VPDB by analysing NBS19 international standards in
233 “Kiel” mode.

234

235 **3.3 Laser analytical system**

236 The laser source is a laser diode with a maximum output power of 30 W and an
237 emission wavelength around 880 nm (JOLD®) connected to an optical fiber 200 μm in
238 diameter with a numerical aperture of 0.22. This laser module is manufactured in
239 large series and generally used as an optical pumping source in solid state lasers; it
240 is efficient at high optical / electrical efficiency (≥30%), inexpensive (<2k€), small
241 (90x50x25 mm) and light (0.25 kg) and is available from many manufacturers. The
242 laser source is mounted on two Peltier modules and a heat sink to control and
243 regulate the temperature of the laser diode and to stabilize its operation in
244 wavelength to around 880 nm at 28°C. The laser output power is controlled by an
245 adjustable current power supply from 0 to 42 A which corresponds to a variable laser
246 power at the optical fiber output from 0 to 25 W. The laser is integrated in a lab-made
247 compact and portable "control box" which also includes switching power supply
248 modules, allowing it to be fitted with either a mains power adapter or a battery
249 (including a car battery) under a large input voltage range. It also includes a user
250 interface and several electronic drivers based on an Arduino® Due single board
251 computer and a color touch screen associated with a color video LCD screen that
252 imaged the surface of the sample. Specific software has been developed to control
253 all laser parameters (current and therefore laser power, temperature, duration of
254 power rise and fall time, continuous or pulse operation, etc.) and accessories. A
255 double security system with two different keys (general ON / OFF, and laser firing
256 authorization) also makes it possible to secure the access to the laser, which is very

257 important given the high power of the laser (class IV laser). The optical fiber from the
258 laser module and the electrical cable for controlling the accessory functions are then
259 connected to an optical unit for shaping, focusing, targeting and viewing the sample.
260 This unit includes an optical system for collimating and focusing the laser beam at
261 the output of the optical fiber. It is composed of two achromats (50 and 100 mm from
262 Thorlabs®) with a focal length of approximately 100 mm corresponding to a laser
263 spot of 400 μm in diameter and a depth of field (assuming $\pm 10\%$ variations on the
264 diameter) of approximately ± 1.0 mm. The optical unit is associated with two laser
265 sighting diodes (@ 630 nm) crossing at the focal point of the power laser beam in the
266 focal plane. The aim of this system is to allow precise targeting of the sample in
267 complete safety. The optical unit is also mounted on a vertical translation system to
268 adjust the focal plane on the surface of the sample, which can have variable
269 thickness. Under the optical unit is then mounted a 45° dichroic separator, which
270 allows the near infrared to be transmitted and visible wavelengths reflected to a color
271 video camera. This camera has a low-pass filter which protects it from laser light
272 reflected or scattered by the sample in order to prevent damage.

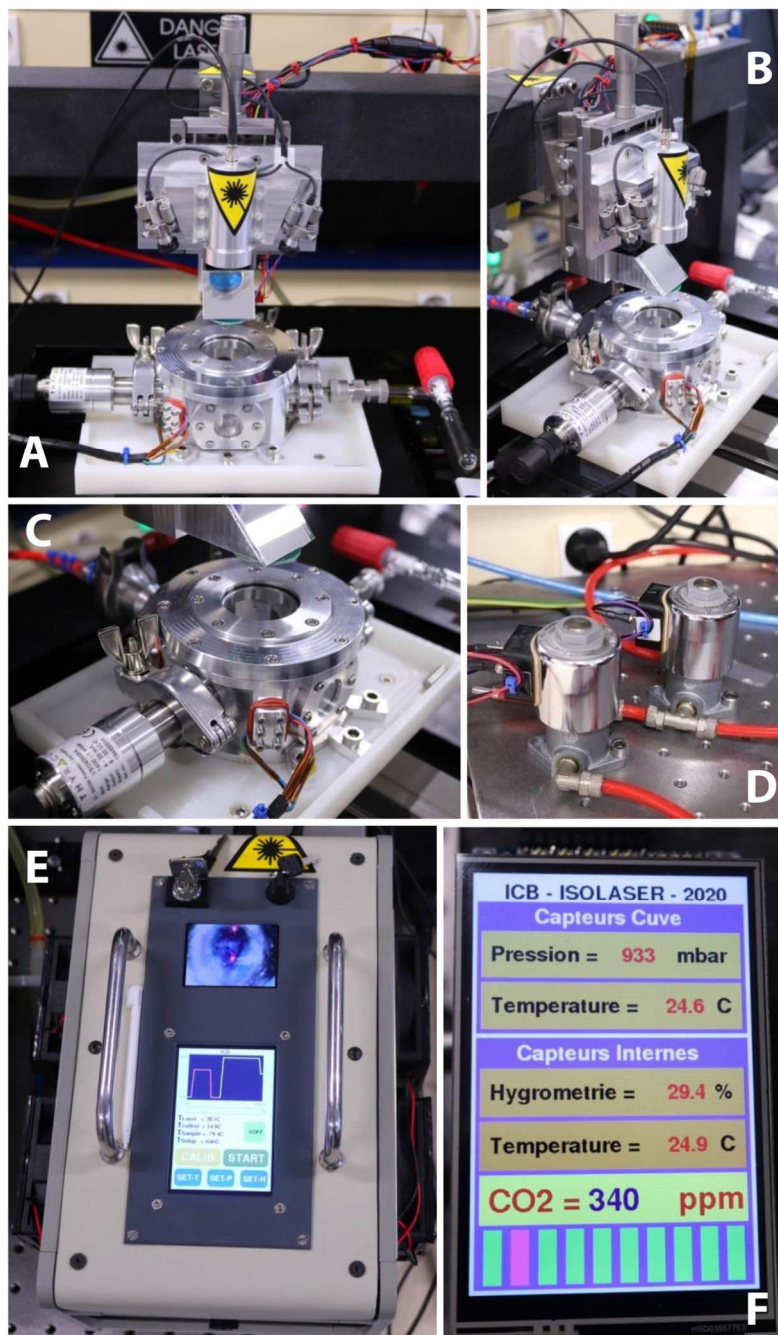
273 The sample is introduced in a Fortal® alloy chamber (Figure 1). It includes on
274 top a large diameter BK7 optical window (50 mm, broadband AR coatings of both
275 faces, Edmund®) and a side window to observe the laser material interaction or for
276 example place other optical sensors (spectrometers, photodiodes).

277 The sample chamber has three ports. (i) the first port is used for evacuating the
278 chamber using a primary vacuum pump or for injecting gas (ambient air, synthetic air,
279 nitrogen, argon, etc.) into the chamber. It includes two solenoid valves to switch from
280 one operating mode to the other. (ii) the second port is connected to a pressure
281 probe (Pirani gauge with range from 1mbar to 1.4bar, Tyracont®). (iii) the third port is
282 used to connect either a glass sample tube or a pump to drive the gas produced, for
283 example, to an optical spectrometer of IRIS or CRDS type.

284 Inside the sample chamber are also arranged several sensors including a
285 thermistor sensor (10k Ω NTC) for measuring the temperature under the sample, a
286 second compact pressure probe (MPX4115, NXP®) and an atmospheric control
287 module capable of measuring the concentration of CO₂ (in ppm), humidity and
288 temperature (SCD30, Sensirion®). This module is designed to work around
289 atmospheric pressure with a slow response time (one acquisition every two seconds,
290 and reliable measurement obtained in one to a few minutes) and does not allow

291 measurement of the evolution of CO₂ in real time. However, it allows the quantity of
292 CO₂ produced during laser irradiation to be quantified after allowing sufficient
293 measurement time. The sample chamber sensors are controlled by a second
294 Arduino® Due module which directly displays the measured data and their variations
295 on a compact color screen. The sample chamber is fitted on a micrometric motorized
296 XY movement platform mounted on an air cushion and controlled by a third Arduino®
297 Due module.

298 Overall, the laser system, presented on the Figure 1, is compact and easily
299 transportable, with a small and light fiber coupled laser diode paired with a compact
300 and portable control box.



301
302
303
304
305
306

Figure 1: Photographs of the laser analytical system installed in the Laboratoire Interdisciplinaire CARNOT, Université de Bourgogne Franche-Comté, France. A and B front and side view of the laser analytical system; C close up view of the sample chamber with glass sample tube port on the right and pressure gage fitting on the left; D solenoid valves allowing to switch from vacuum to controlled atmosphere; E lab-made compact "control box"; F lab-made color screen data display.

307

3.4 Assessment of the calcination yield

308

309 The experimental device makes it possible to measure the quantity of CO₂
310 produced by calcination and also to evaluate the shape and appearance of the areas
311 impacted by the interaction between the laser and the sample. The CO₂ sensor used
312 is designed to operate around atmospheric pressure. A specific protocol is therefore

313 applied. For each sample tested, the chamber and the main optical window are first
314 cleaned. The sample is then placed in the chamber under primary vacuum; the
315 height is adjusted so that the focal plane of the focusing lens is positioned on the
316 surface of the sample. The chamber is then isolated from the pump and an air inlet
317 allows the pressure to rise to atmospheric pressure. The air or gas inlet valve is then
318 closed. The information from the sensors is then read after a stabilization time of 5
319 min (imposed by the infrared CO₂ sensor). The laser exposure is then carried out at
320 desired intensity and duration. The CO₂ is monitored 5 minutes after laser exposition,
321 permitting quantification of the CO₂ released by the increase in CO₂ above ambient
322 atmospheric concentration. The protocol is repeated for the next measurement with,
323 if necessary, a displacement of the sample using the XY movement platform.
324 Observations of the Heat Affected Zone (HAZ) are carried out outside the sample
325 chamber using a binocular microscope.

326

327 **3.5 Gas collection for isotopic measurements**

328 Laser calcination for isotopic measurements were all performed at a laser
329 power of 25 W (equivalent to an intensity of 20 kW/cm² on the sample surface). The
330 sample chamber and the sampling tube were first evacuated for 3 minutes. The
331 sampling tube valve was then closed. The laser was then turned on and the sample
332 was rastered until 300 mbar of gas was produced (corresponding to a surface of
333 around 1 cm²). When the desired pressure is obtained (between 1 and 2 minutes),
334 the laser was turned off and the evolved gas transferred to the sample tube by gas
335 pressure equilibration (2 minutes).

336

337 **3.6 μXRF**

338 μXRF elemental mapping of the heat affected zone (HAZ) was performed using a
339 Bruker M4 Tornado μXRF fast mapping instrument operating under vacuum (20
340 mbar) at 50kV and 600μA with a dwell time of 6 ms/pixel. Data were visualized in
341 relative intensities using the Bruker Tornado software with spectral deconvolution
342 applied.

343

344 **4. Results**

345 **4.1 Calcination threshold**

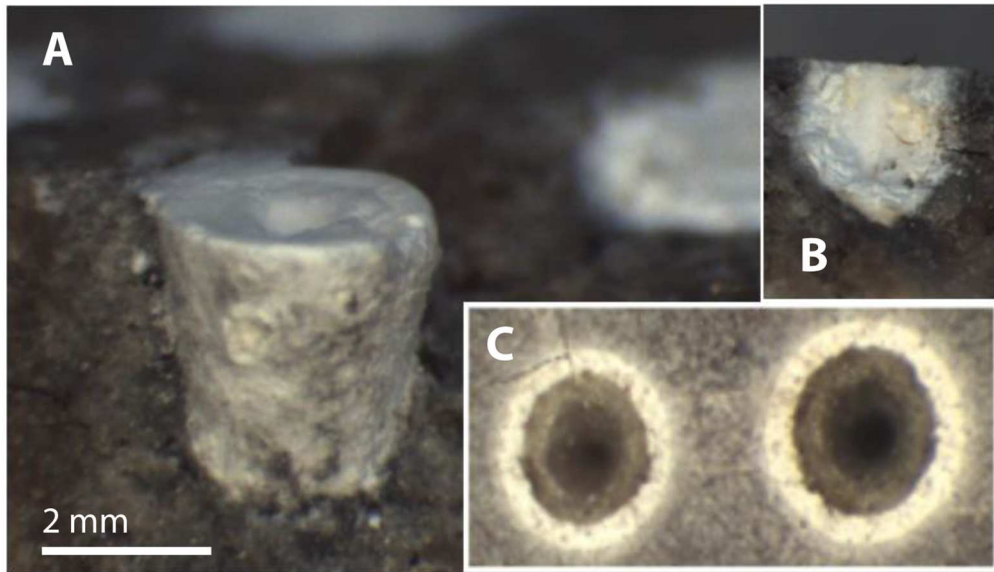
346 The heat affected zone (HAZ) is a first order means of describing laser-material
347 interaction. This HAZ corresponds to the volume of material where the interaction
348 between the laser light and the irradiated material causes a change in color, volume
349 or density, or even in chemical composition. The area of this zone can be smaller
350 than the laser spot or larger depending on the temperature locally reached in the
351 material. In general, the material transformation effects take place when an intensity
352 threshold is reached. This threshold depends on the ensemble of optical, thermal and
353 mechanical parameters of the irradiated material. The materials considered in this
354 work being very diverse, variable transformation thresholds can be expected.
355 Likewise, they are relatively inhomogeneous in general and it is therefore necessary
356 to repeat each measurement point to obtain a statistic understanding of the
357 probability of transformation. Calcination is primarily assessed based on the
358 appearance of HAZ laser pits after individual laser pulses (Figures 2 and 4). To
359 achieve a representative laser shot, the laser current was adjusted for a 5s pulse,
360 with 1s of rise and fall time on either side; the optical pulse duration due to current
361 threshold for laser emission can be approximated to a constant to 5s.

362 The probabilities of inducing calcination were measured according to the laser
363 intensity applied on the sample following the method describe in paragraph 3.4. We
364 present below the results for the Death Valley Stromatolite (SDV, sample 8) as it is a
365 homogeneous sample in terms of mineralogy. Figure 2 shows photographs of the
366 HAZ laser pits at the surface and at depth obtained using a laser intensity of 13 kW /
367 cm² over 5 s; the white area is lime which crumbles into a very fine white powder
368 after hydration.

369

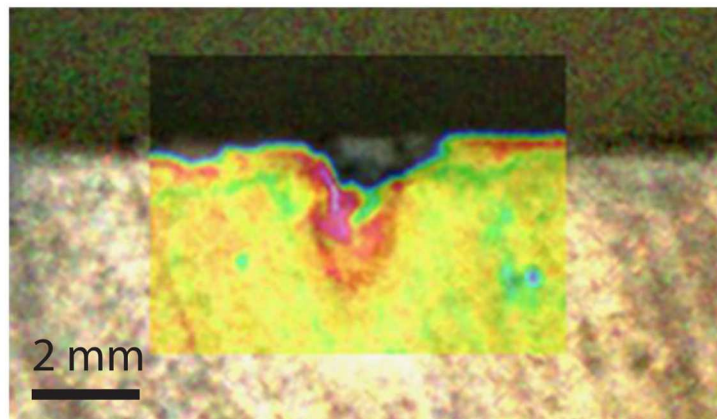
370

371



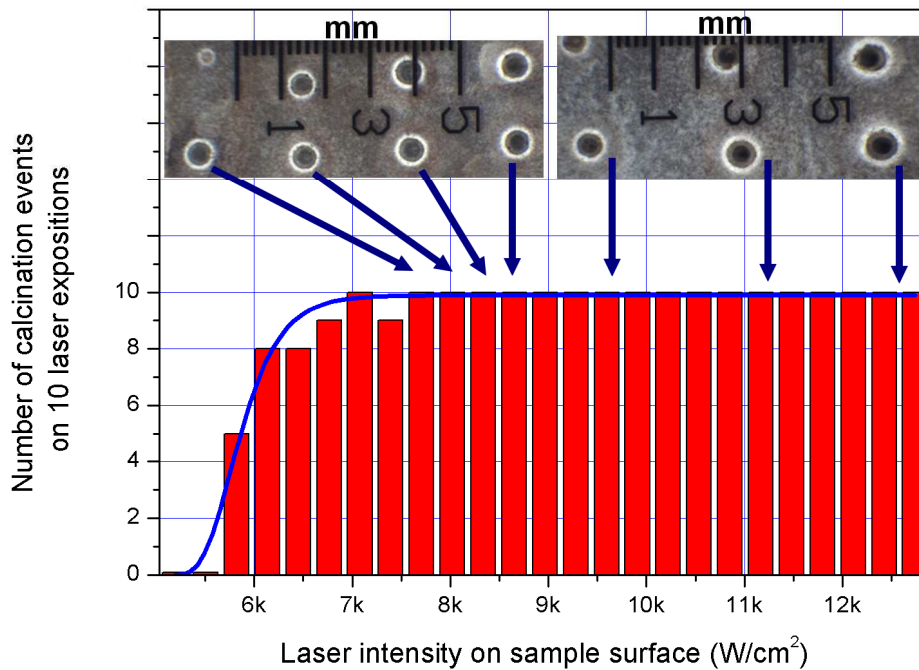
372
 373 **Figure 2: Photography of sample SDV after treatment of 16 W of laser light corresponding to an intensity of 13**
 374 **kw/cm² -5 s. The diameter of HAZ is around 2 mm and depth around 3-4 mm (30 A/5 s). A and B side view, C front**
 375 **view.**

376
 377 Figure 3 shows a μ XRF chemical map performed in side view on a HAZ of this
 378 sample. Locally increased Ca intensities reveal the presence of CaO, which has a
 379 higher volumetric Ca concentration relative to (Ca-Mg)CO₃. It can be seen that CaO
 380 production is focused on the crater walls and floor, and does not appear to extend
 381 more than a mm from the crater wall into the bulk sample.



382
 383 **Figure 3: μ XRF Ca chemical mapping (relative color scale) in side view of a HAZ of sample SDV after calcination.**
 384

385 Figure 4 shows the histogram of calcination (inferred by the appearance of the
 386 HAZ laser pit) as a function of the intensity. The experiment was made 10 times
 387 for each intensity and the height of the bar gives the number of events observed
 388 at each intensity.



390

391

392

393

Figure 4: Histogram of calcinations events as a function of laser intensity for the SDV sample at a constant exposure time of 5s.

394

395

396

397

398

399

400

401

402

403

404

405

406

4.2 CO₂ release efficiency

407

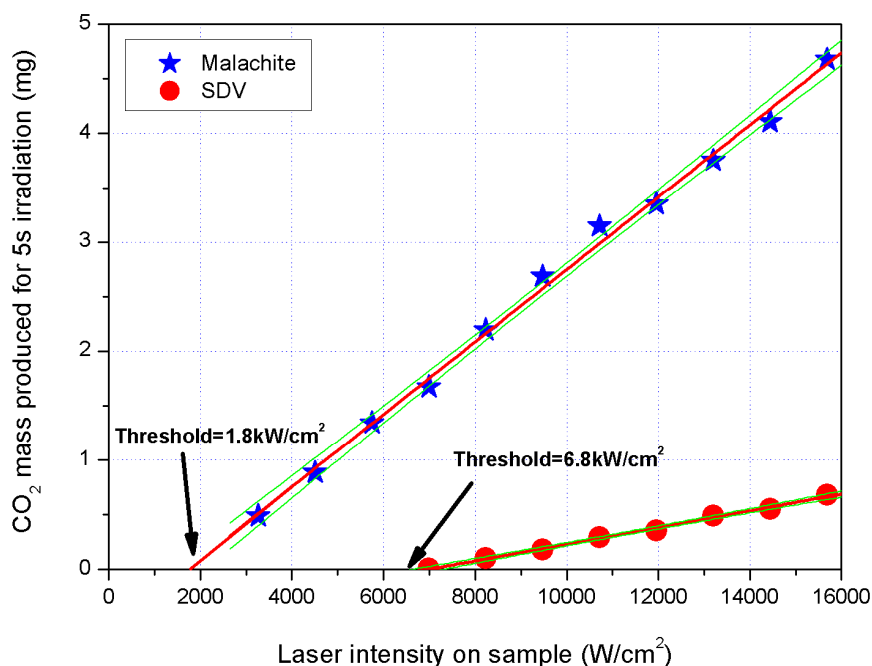
408

409

We estimate the amount of CO₂ released for variable parameters of laser intensity and exposure duration in order to verify if CO₂ production is linear as a function of these parameters and to assess thresholds and efficiency for the different studied

410 materials. For this, we used 2 different samples: malachite and SDV-stromatolite.
411 The measurements are made in ppm and were converted into a mass of CO₂ using
412 the known volume of the chamber (115 cm³). In our experimental setup, 1 ppm
413 corresponds to 2.03 10⁻⁴ mg of CO₂.

414 Figure 5 shows the mass of CO₂ produced as a function of laser intensity for a
415 constant exposure time of 5 s. The 2 samples show a linear variation in the mass of
416 CO₂ produced by laser calcination (R above 0.99). The thresholds and slopes
417 calculated by linear regression are very different from one sample to another. The
418 thresholds are 2 and 7 kW/cm² and the slopes are 3.3 10⁻⁴ and 0.8 10⁻⁴ mg/(W/cm²)
419 for Malachite and SDV, respectively. These differences are expected with materials
420 whose coefficient of reflection and absorption can strongly vary from one chemical
421 composition to another (Othman et al., 2019). Likewise, the thermal properties and
422 enthalpy of calcination will also vary greatly from one chemical composition and
423 structure to another. However, the linear behaviour of CO₂ release as a function of
424 laser intensity is verified in each case.



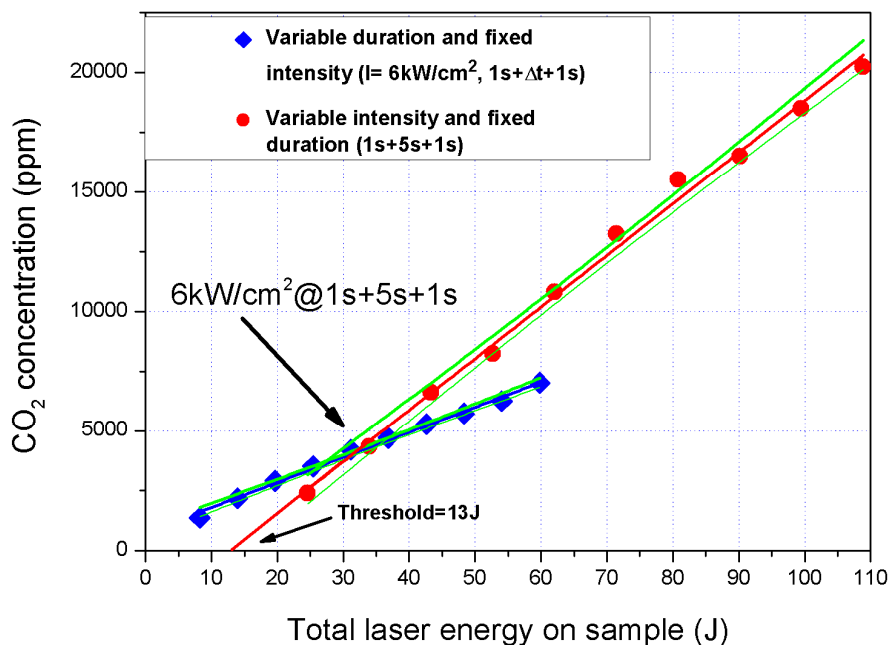
425

426 **Figure 5: Mass of CO₂ (mg) produced as a function of laser intensity (W/cm²) on the sample for 5 s exposure time for**
427 **malachite and SDV dolomicrite (red line: linear fit, green lines: 95% confidence intervals)**

428

429 Further experiments were carried out to determine how the different parameters
430 (laser intensity vs. the duration of exposure) contribute to optimization of the

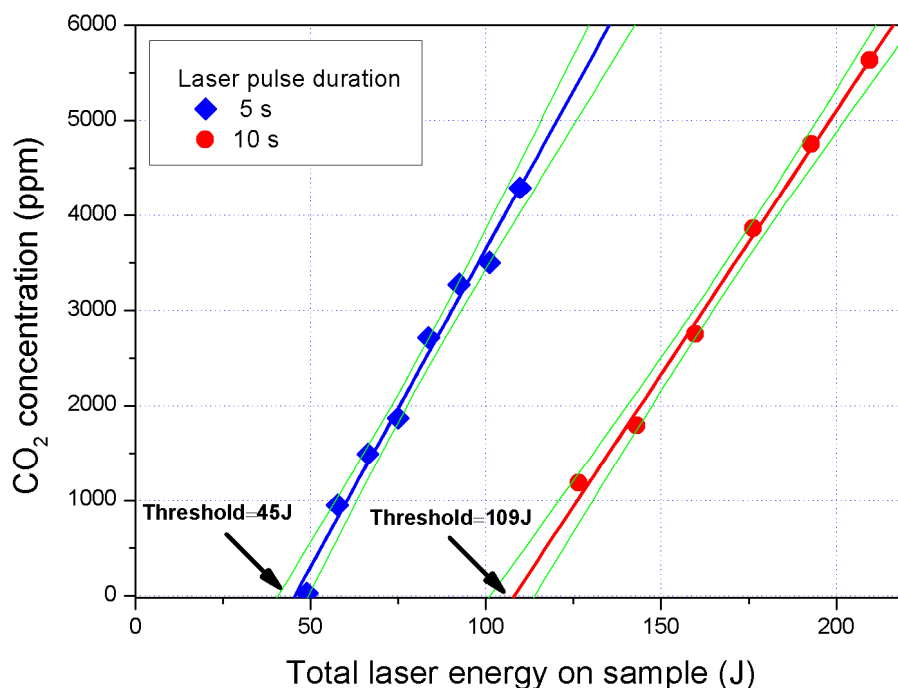
431 calcination process. Figure 6 and Figure 7 show two examples of results obtained for
 432 two different materials in terms of calcination efficiency. Figure 8 shows the CO₂
 433 released (in ppm) from Malachite as a function of the incident laser energy by
 434 comparing two heating modes: a constant exposure time (5 s) with variable intensity
 435 vs. a fixed intensity (6 kW/cm²) with variable exposure time (1 to 10 s in addition to
 436 rise and fall times of 1 s each). The incident energy is simply calculated by the
 437 product of the incident laser power multiplied by the exposure time. We observe two
 438 regression lines ($R^2 = 0.99$) with a difference of a factor of 2 in their slopes (Fig. 8).
 439 The two curves intersect close to the typical operating conditions (i.e. $I = 6 \text{ kW/cm}^2$
 440 and $\Delta t = 5 \text{ s}$). These differences demonstrate that it is much more efficient to
 441 increase incident laser power than exposure time, and hence that working with high
 442 laser intensities over shorter exposure times constitutes the most efficient operating
 443 approach. Moreover, it is more difficult to reach the calcination temperature, to
 444 maintain it and to provide the necessary energy of enthalpy with a longer exposure
 445 time than with a stronger intensity. In the case of long exposure time, thermal losses
 446 induced by thermal conductivity and diffusivity are also increased.



447
 448 **Figure 6: Evaluation with Malachite of the CO₂ concentration as a function of the incident laser energy for two**
 449 **different approaches: at constant exposure time and adjustable intensity and at fixed intensity and variable exposure**
 450 **time (red and blue lines: linear fit, green lines: 95% confidence intervals).**

451

452 Malachite has a very favourable threshold and slope for CO₂ production.
 453 However, this is not a common type of carbonate in comparison to calcite or
 454 dolomite, which have more interest as paleoenvironmental archives. Accordingly, the
 455 same kind of measurements were applied to the SDV sample, with two different fixed
 456 exposure times (5 and 10 s) and variable laser intensity. In Figure 7 the quantity of
 457 CO₂ produced is expressed as a function of the incident laser energy. We observe
 458 again two regression lines ($R^2 = 0.99$) with similar slopes but very different
 459 thresholds. In the case of SDV dolomite, variation in exposure duration does not
 460 change the linear relationship between laser energy and CO₂ production (reduction
 461 by about 15% between 5 s and 10 s) but the threshold for calcination is more than
 462 doubled with an increase of 140%. Moreover, we notice that with the SDV sample the
 463 intensity threshold for calcination is very high compared to malachite (see Figure 6).
 464 The calcination threshold is therefore much more difficult to reach for dolomite
 465 compared to malachite. The laser intensity must all the higher, but similar to the case
 466 of malachite, it is again more efficient to favour higher intensity than longer exposure
 467 time, the latter being associated with higher thermal losses.



468

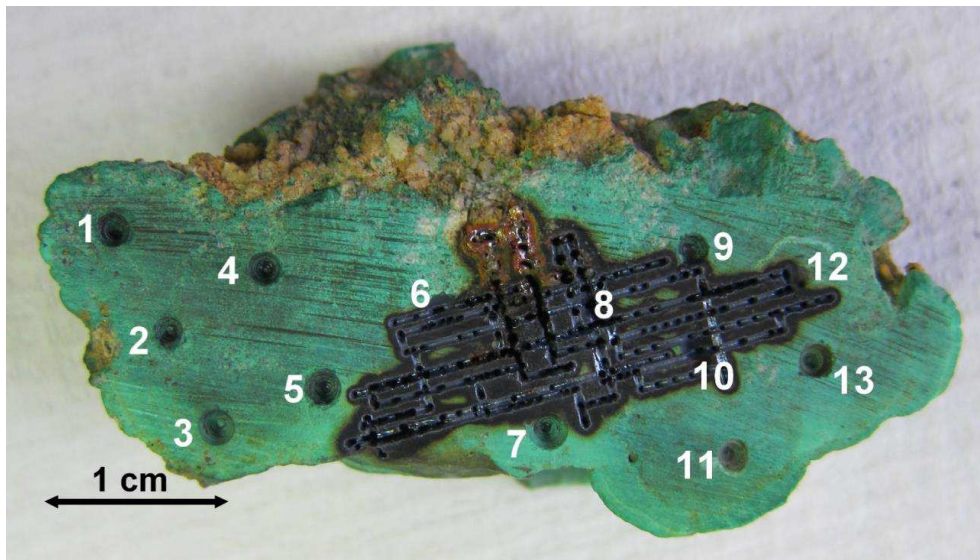
469 **Figure 7: Concentration of CO₂ as a function of incident laser energy with SDV for two exposure times and variable**
 470 **intensity (red and blue lines: linear fit, green lines: 95% confidence interval).**

471

472

4.3 Isotopic results

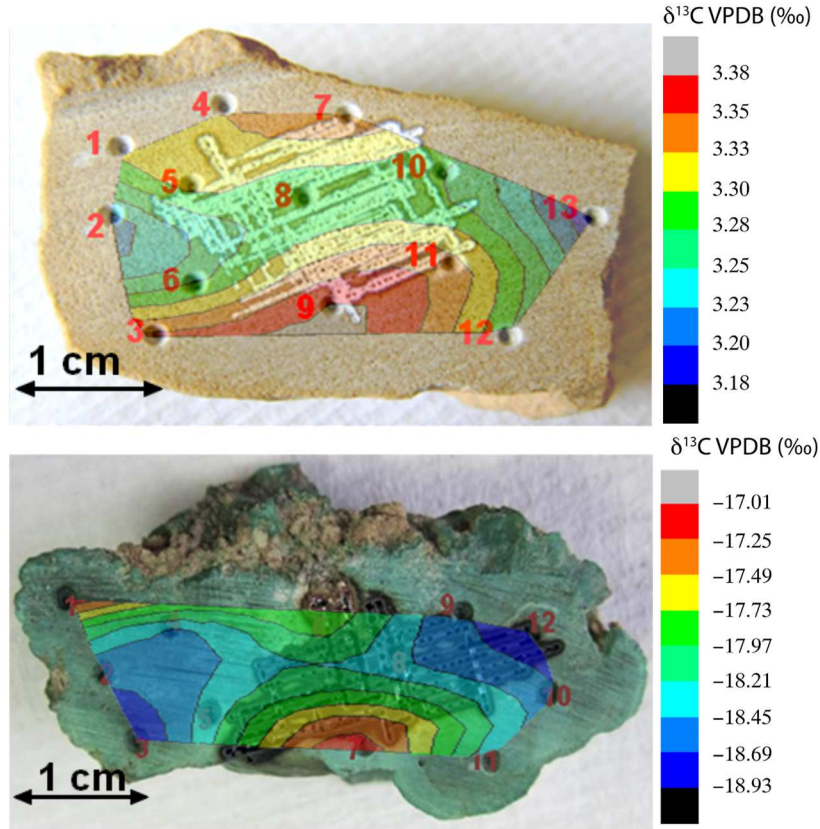
473 All samples were first micro-drilled several times along their surface before being
474 irradiated using the laser system (Figure 8). Isotopic results of both techniques are
475 given in Table 2.



476
477 **Figure 8: Malachite sample after micro-drilling and laser irradiation**
478

479 **4.3.1 Isotopic sample heterogeneity and analytical reproducibility**

480 Spatial variability in sample isotopic composition as determined by micro-drilling
481 and classic IRMS analysis is quantified in Table 2 by the standard deviation of $\delta^{13}\text{C}$
482 and $\delta^{18}\text{O}$ and represented graphically for calcite and malachite samples in Figure 9.
483



484
485
486
487
488
489

Figure 9: Photographs of sample 2 (SDV Dolomite) and sample 6 (Malachite). Each number represents the microdrill subsample analyzed to estimate the isotopic homogeneity in $\delta^{13}\text{C}$ and $\delta^{18}\text{O}$ of the sample. The white or dark layers correspond to the holes made by the laser as described below. The color map with color scale on the right presents the mathematical fitting of isotopic variations on the sample surface after “microdrill” analyses.

	Classical technique					Laser calcination								
	Number of microdrilling analyses	$\delta^{13}\text{C}$ ‰ VPDB	Standard deviation (1σ)	$\delta^{18}\text{O}$ ‰ VPDB	Standard deviation (1σ)	Number of laser calcination repeats	$\delta^{13}\text{C}$ ‰ VPDB	Standard deviation (1σ)	$\delta^{18}\text{O}$ ‰ VPDB	Standard deviation (1σ)	m/z 44 (mV) CO_2	m/z 40 (mV) Ar	m/z 28 (mV) N_2	m/z 32 (mV) O_2
Calcite 1	6	4.90	0.66	-3.55	0.39	1	3.96		-13.73		2221	32	2242	573
Calcite 2	7	-0.64	1.33	-14.29	0.57	1	-1.51		-22.59		ND	ND	ND	ND
Dolomite 1	9	2.31	0.16	-6.01	0.18	1	1.78		-15.50		2042	38	2303	527
Dolomite 2	13	3.30	0.05	-1.74	0.16	2	2.62	0.61	-12.34	1.19	2867	28	1877	416
Sidérit	9	-12.22	0.14	-14.57	0.27	2	-	0.21	-22.29	0.20	2642	26	1778	284

e							11.38							
Malachite	13	-18.24	0.66	-3.30	0.23	3	-18.00	0.27	-13.76	1.40	2683	27	1563	463
Rhodocrosite	16	-12.33	0.52	-4.53	0.17	1	-12.27		-9.64		1878	115	6089	1348
SDV	5	-3.01	0.07	-6.05	0.10	5	-2.53	0.17	-14.92	0.19	ND	ND	ND	ND

490

491

492

493

494

495

Table 2: Stable isotope compositions of carbon and oxygen measured after classical “acid technique” and laser CO₂ released experiments performed on 1cm² of samples and gas relative concentration of samples collected after laser calcination. ND: non-determined.

496

497

498

499

500

501

502

503

504

505

506

507

508

509

510

511

4.3.2 Carbon isotope inter-calibration

512

513

Figure 10 reports the $\delta^{13}\text{C}$ values measured using the state-of-the-art acid technique versus the new laser protocol.

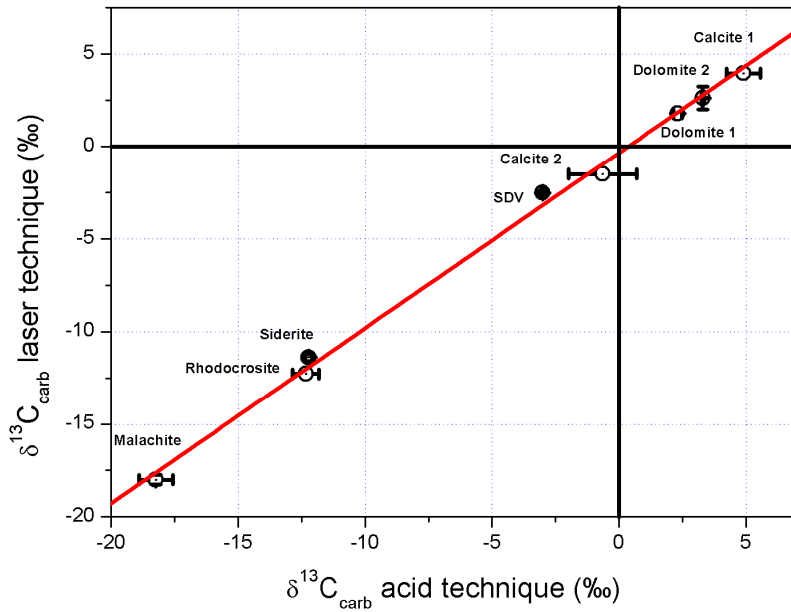


Figure 10: Carbon isotope results for carbonates after laser and acid treatments in ‰ VPDB.

514
515
516
517
518
519
520
521
522
523

Carbon isotope values determined by both techniques compared very well, with a correlation coefficient of 0.996 and a slope of 0.95. The intercept of the linear regression is close to the origin, with an offset of -0.35‰, which falls in the range of sample $\delta^{13}\text{C}$ inhomogeneity describe in paragraph 4.3.1 (see also Table 2). Moreover, no systematic offset is observed between both techniques (Table 3) and the absolute difference is very close to zero with a mean value of $-0.17 \pm 0.67\text{‰}$ (1σ).

isotopic differences between laser and classical technique (laser - acid)						
	$\delta^{13}\text{C}$ ‰ VPDB	Mean	Standard deviation (1σ)	$\delta^{18}\text{O}$ ‰ VPDB	Mean	Standard deviation (1σ)
Calcite 1	-0.94	-0.17	0.67	10.18	9.38	1.12
Calcite 2	-0.87			8.30		
Dolomite 1	-0.53			9.49		
Dolomite 2	-0.68			10.60		
Sid�rite	0.84			7.72		
Malachite	0.24			10.46		
Rhodocrosite	0.06					
SDV	0.48			8.88		

524
525
526

Table 3: Measured isotopic differences between laser and classical techniques used in this study to measured carbon and oxygen isotopes of carbonates.

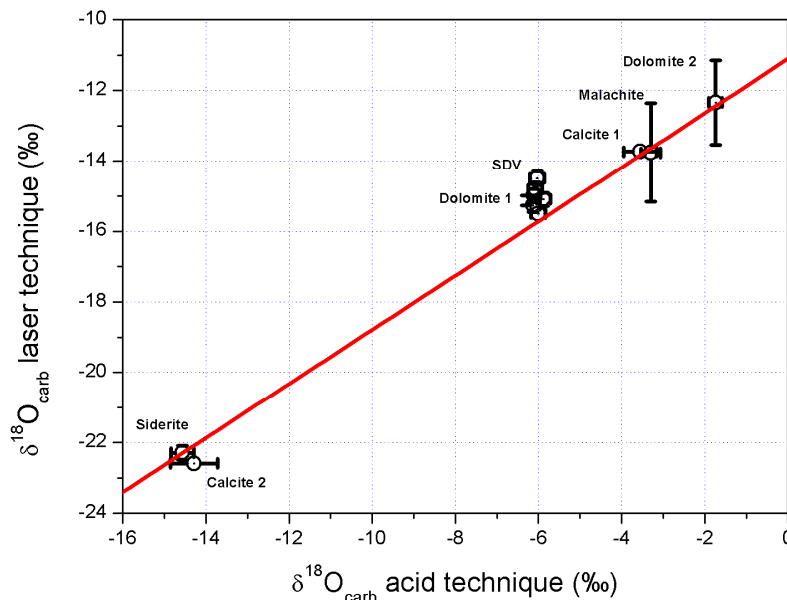
527

528 Overall, the intercalibrations demonstrate the robustness of the laser
529 calcination method, without any noticeable effect related to the mineralogy of the
530 samples over a large range of isotopic compositions (between around -18 to 5‰),
531 encompassing most of the variability of Earth's natural carbonates.

532

533 4.3.3 Oxygen isotopes inter-calibration

534 Figure 11 reports the $\delta^{18}\text{O}$ values measured using the state-of-the-art acid
535 technique versus the new laser protocol. Notice here that the $\delta^{18}\text{O}$ value of
536 Rhodochrosite is excluded from this comparison due to strong O_2 -bearing air
537 contamination (see Table 2).



538

539 **Figure 11: Oxygen isotopes results of carbonates (Rhodochrosite excluded) after laser and acid treatments in ‰**
540 **VPDB.**

541

542 Both techniques compared well, with a correlation coefficient of 0.986 over a
543 large range of isotopic compositions (spanning ca. -15 to -2‰). However, the slope
544 of the linear regression fit is significantly different from 1 with a value of 0.77. The
545 intercept is also significantly deviated from the origin with an intercept at -10.88‰,
546 the laser data being systematically enriched in ^{16}O . This systematic difference is also
547 illustrated in Table 3 with an absolute difference between both techniques (i.e. laser –
548 acid) of $9.38 \pm 1.12\%$ (1σ).

549 Therefore, the intercalibration is also favorable for oxygen isotopes, over a large
550 range of carbonate lattice configurations and isotopic compositions. However, a
551 correction factor, reflecting a laser calcination isotopic equilibrium or pseudo-
552 equilibrium between CaO and CO₂, has to be applied to report the results on the
553 VPDP scale. This isotopic effect has yet to be characterized in detail and should be
554 considered in more detail in future studies in order to verify if a single correction
555 factor can be applied on serial analyses of samples.

556

557 **5. Discussion**

558 The new fiber coupled laser diode technique described here compares well in
559 performance with previous laser-based methods for carbonate isotope analyses
560 (Smalley et al., 1989; Smalley et al., 1992; Sharp, 1992; Sharp and Cerling, 1996;
561 Cerling and Sharp, 1996; Spötl and Matthey, 2006). Table 4 summarises the results
562 of this study and six previous published techniques, based on either Nd:YAG or CO₂
563 lasers, in terms of spot size, gas purification steps, analysis time, reproducibility, and
564 apparent isotopic shifts between laser ablation and conventional acid digestion
565 analysis. The fiber coupled laser diode technique examined in this study shows a 1-
566 standard-deviation reproducibility that is effectively equivalent to that obtained by
567 prior published laser ablation techniques for $\delta^{13}\text{C}$ (0.3‰ vs. 0.2 to 0.5‰ in previous
568 studies), and only slightly greater relative to prior techniques for $\delta^{18}\text{O}$ (0.7‰ vs. 0.1 to
569 0.5‰ in previous studies). For $\delta^{13}\text{C}$ determination, the fiber coupled laser diode
570 method shows excellent agreement with results obtained by conventional acid
571 digestion analyses. However, in the case of $\delta^{18}\text{O}$, we observed a strong isotopic shift
572 (-9.4‰ \pm 1.1) relative to values obtained by conventional acid digestion analyses,
573 which was relatively constant across the different replicates and minerals examined,
574 permitting the application of a constant correction factor for the conditions examined
575 herein. Such an important degree of fractionation of oxygen isotopes during laser
576 ablation has been observed previously and attributed to the fact that only 2/3 of the
577 oxygen atoms are removed from the carbonate during laser heating (equation (1))
578 (Sharma and Clayton, 1965). However, we notice that compared to previously
579 published techniques (Figure 4), the partitioning seems to be constant throughout our
580 set of samples, but that the value of this offset is higher than previously observed.
581 This shift warrants further examination in future work; additional experiments may

582 resolve whether it represents a kinetic isotope or partial reaction effect, in which case
 583 the shift might be modified under different laser ablation conditions such as the
 584 intensity delivered at the focal point or duration (see supplementary information for a
 585 laser type comparison), or whether it represents an equilibrium fractionation between
 586 CO₂ and CaO (and/or other relevant species) that would remain largely constant if
 587 equilibrium conditions were consistently achieved. Mass scans revealed no
 588 significant amount of carbon monoxide (data not shown), which had previously been
 589 suggested as a possible issue for laser pulses of ≥1s duration (Powell and Kyser,
 590 1991). The ratio of ions at m/z 28 and 32, reflecting the O₂ / N₂ ratios of analysed
 591 sample gases (Table 2), were very close to the atmospheric ratio of 4, pointing to
 592 trace air in the system rather than any significant CO production.

593
 594

	Smalley et al., 1989	Smalley et al., 1992	Sharp, 1992	Sharp and Cerling, 1996	Cerling and Sharp, 1996	Spötl and Matthey, 2006	This study
Laser type	Nd:YAG	Nd:YAG	CO ₂	CO ₂	CO ₂	CO ₂	Laser diode
minimum spot size	10 µm	35 µm	80 µm	100 to 200 µm	200 to 250 µm	300 µm	400 µm
Gas purification steps	cold trap	cold trap	cold trap	continuous flow He-GC	cold trap and continuous flow He-GC	continuous flow He-GC	direct gas injection in mass spec
Total time of one analysis	nd	30 minutes	nd	nd	nd	3 minutes	few minutes

Isotopic differences between laser and conventional acid digestion	1.7 (calcite) to 2.5 (aragonite) ‰ for $\delta^{18}\text{O}$; no correction for $\delta^{13}\text{C}$	1.2‰ for $\delta^{18}\text{O}$; -0.8‰ for $\delta^{13}\text{C}$	nd	0.3 (calcite) to 2.1 (siderite) ‰ for $\delta^{18}\text{O}$; 0.05±0.3 ‰ for $\delta^{13}\text{C}$ (excluding siderite at ca. 2‰)	0.68±0.67 ‰ for $\delta^{13}\text{C}$ (oxygen isotopes are a mixture of CO_3 and PO_4 in this case)	-1.14‰ for $\delta^{18}\text{O}$; 0.14‰ for $\delta^{13}\text{C}$	-9.38 ±1.12‰ for $\delta^{18}\text{O}$; -0.17 ±0.67‰ for $\delta^{13}\text{C}$
Reproducibility of replicate laser analyses (1σ)	±0.2‰ for $\delta^{18}\text{O}$ and $\delta^{13}\text{C}$	±0.4‰ for $\delta^{18}\text{O}$; ±0.2‰ for $\delta^{13}\text{C}$	±0.1‰ for $\delta^{18}\text{O}$; ±0.2‰ for $\delta^{13}\text{C}$	±0.29‰ for $\delta^{18}\text{O}$; ±0.19‰ for $\delta^{13}\text{C}$	±0.5‰ for $\delta^{18}\text{O}$ and $\delta^{13}\text{C}$	±0.3‰ for $\delta^{18}\text{O}$ and ±0.2‰ for $\delta^{13}\text{C}$	±0.7‰ for $\delta^{18}\text{O}$ and ±0.3‰ for $\delta^{13}\text{C}$
Type of carbonates analyzed	calcite and aragonite	calcite and dolomite	metamorphic calcite and dolomite	calcite, dolomite, magnesite, rhodocrosite, siderite and smithsonite	Tooth enamel	Carrara marble	calcite, dolomite, malachite, rhodocrosite, siderite

Table 4: Comparison of different laser analytical methods applied to carbonate stable isotope analyses.

595
596
597

598 While the analytical performance of the fiber coupled diode laser calcination
599 system is comparable to previous systems, it has several additional advantages over
600 previous systems. First, the system examined in this study appeared to be largely
601 immune to matrix effects, at the cm^2 scale of analysis presented here, providing
602 robust results for a wide range of carbonate minerals. Additionally, no gas purification
603 steps nor consumable reagents were required, which opens the door to systems of
604 significantly reduced complexity. Furthermore, fiber coupled diode lasers are readily
605 available, highly compact, affordable, and highly adjustable in terms of laser intensity
606 and shot duration. This combination of characteristics provides for a highly compact
607 laser ablation system (benchtop for the current setup), and more importantly, may
608 enable novel applications in the future. For example, such a system could easily be
609 made portable, deployable on-site or in the field, where samples could be prepared
610 as glass vials containing CO_2 gas ready for later offline IRMS analyses after laser
611 calcination of centimetric surfaces. Even more exciting is the potential of coupling

612 such a system to a sufficiently compact spectroscopy-based CO₂ isotope ratio
613 analyzer (e.g., CRDS or IRIS) such that a single highly compact (e.g., automobile-
614 portable) system would be capable of producing high-quality spatially-resolved C and
615 O isotope compositions of carbonate minerals directly in the field, or integrated as an
616 additional analytical component in multi-parameter core scanner device. Future
617 developments also include the possibility of down-scaling isotopic measurements in
618 the micro-metric range of analysis (i.e. single laser pulses) after careful examinations
619 of possible micro-scale isotopic effects due to impurities, inclusions or variations in
620 crystal lattice.

621

622 **6. Conclusions**

623 We report that the use of the coupled diode laser calcination system for
624 analyzing the stable carbon and oxygen isotopic composition of carbonates gives
625 reproducible results that can be scaled to the state of the art acid dissolution
626 technique without correction for $\delta^{13}\text{C}$ and after calibration for $\delta^{18}\text{O}$. Moreover,
627 intercalibration results demonstrate that this new laser calcination method, at the
628 centimeter scale, compares well with classical methods for carbonates of different
629 mineralogies and over a large range of isotopic compositions for both carbon and
630 oxygen isotopes.

631 This new calcination method using a fiber coupled laser diode for the stable
632 isotope analysis of carbonate has several important advantages over previous
633 methods. Compared to acid dissolution techniques, this method drastically reduces
634 the time of analysis while also offering spatially resolved isotopic characterization.
635 While previous automated CO₂ laser ablation techniques have been proven to
636 efficiently perform high resolution $\delta^{18}\text{O}$ and $\delta^{13}\text{C}$ measurements of laminated
637 speleothems (Spötl and Matthey, 2006; McDermott, 2005; Cosford et al., 2008; Hodge
638 et al., 2008; Cosford et al., 2009; Cosford et al., 2010; Baker et al., 2011; Baldini et
639 al., 2015), the system presented here extends the range of possible analyses to
640 other type of carbonate samples using a single fiber coupled laser diode-induced
641 calcination module. Furthermore, fiber coupled diode lasers are highly compact
642 compared to previous laser systems and can be paired with field-deployable
643 CRDS/IRIS optical-mass spectrometers, opening the door to novel on-site or in the
644 field applications in the near future.

645

646 **Acknowledgements**

647 This work is a contribution to the “Investissements SATT SAYENS” project
648 ISOLASER and was also supported by the Observatoire des Sciences de l’Univers
649 Terre Homme Environnement Temps Astronomie de Franche-Comté-Bourgogne
650 (OSU THETA), and by the FEDER Bourgogne Franche-Comté. The authors would
651 like to thank SATT Ouest for their assistance with this project. The authors also
652 would like to apologise to the LGO ICP-MS laboratory for having exploded a laser
653 ablation cell and to the IPGP stable isotope laboratory for inducing temporary
654 blindness during early tests. We also thank Céline Liorzou for her assistance with
655 early tests. Jerome Thomas is warmly acknowledged for providing access to the
656 Dijon Museum collection of minerals. Sofiane Lazali is acknowledged for his initial
657 work on sorting and micro-drilling the samples of this study. Baptiste Paulmier is
658 acknowledged for his work on the electronic parts of the system. We thank Craig
659 Smalley and an anonymous referee for their constructive reviews and Michael E.
660 Böttcher for handling this contribution.

661

662 **References:**

663 Berner, R. A., Lasaga, A. C., & Garrels, R. M. (1983). The carbonate-silicate
664 geochemical cycle and its effect on atmospheric carbon dioxide over the past 100
665 million years. *AmJS*, 283(7), 641-683.

666 Walker, J. C., Hays, P. B., & Kasting, J. F. (1981). A negative feedback
667 mechanism for the long-term stabilization of Earth's surface temperature. *Journal of*
668 *Geophysical Research: Oceans*, 86(C10), 9776-9782.

669 McCrea, J. M. (1950). On the isotopic chemistry of carbonates and a
670 paleotemperature scale. *The Journal of Chemical Physics*, 18(6), 849-857.

671 Garcia-Anton, E., Cuezva, S., Fernandez-Cortes, A., Benavente, D., &
672 Sanchez-Moral, S. (2014). Main drivers of diffusive and advective processes of CO₂-
673 gas exchange between a shallow vadose zone and the atmosphere. *International*
674 *Journal of Greenhouse Gas Control*, 21, 113-129.

675 Rizzo, A. L., Jost, H. J., Caracausi, A., Paonita, A., Liotta, M., & Martelli, M.
676 (2014). Real-time measurements of the concentration and isotope composition of
677 atmospheric and volcanic CO₂ at Mount Etna (Italy). *Geophysical Research*
678 *Letters*, 41(7), 2382-2389.

679 Fischer, T. P., & Lopez, T. M. (2016). First airborne samples of a volcanic
680 plume for $\delta^{13}\text{C}$ of CO_2 determinations. *Geophysical Research Letters*, *43*(7), 3272-
681 3279.

682 Smalley, P. C., Stijfhoorn, D. E., Råheim, A., Johansen, H., & Dickson, J. A. D.
683 (1989). The laser microprobe and its application to the study of C and O isotopes in
684 calcite and aragonite. *Sedimentary Geology*, *65*(3-4), 211-221.

685 Smalley, P. C., Maile, C. N., Coleman, M. L., & Rouse, J. E. (1992). LASSIE
686 (laser ablation sampler for stable isotope extraction) applied to carbonate
687 minerals. *Chemical Geology: Isotope Geoscience section*, *101*(1-2), 43-52.

688 Sharp, Z. D. (1992). In situ laser microprobe techniques for stable isotope
689 analysis. *Chemical Geology: Isotope Geoscience section*, *101*(1-2), 3-19.

690 Sharp, Z. D., & Cerling, T. E. (1996). A laser GC-IRMS technique for in situ
691 stable isotope analyses of carbonates and phosphates. *Geochimica et*
692 *Cosmochimica Acta*, *60*(15), 2909-2916.

693 Cerling, T. E., & Sharp, Z. D. (1996). Stable carbon and oxygen isotope
694 analysis of fossil tooth enamel using laser ablation. *Palaeogeography,*
695 *Palaeoclimatology, Palaeoecology*, *126*(1-2), 173-186.

696 Spötl, C., & Matthey, D. (2006). Stable isotope microsampling of speleothems for
697 palaeoenvironmental studies: a comparison of microdrill, micromill and laser ablation
698 techniques. *Chemical Geology*, *235*(1-2), 48-58.

699 McDermott, F. (2005) Centennial-scale Holocene climate variability revealed
700 by a high-resolution speleothem delta O-18 record from SW Ireland. *Science*, *309*,
701 1816-1816.

702 Cosford, J., Qing, H., Eglington, B., Matthey, D., Yuan, D., Zhang, M. & Cheng,
703 H. (2008) East Asian monsoon variability since the Mid-Holocene recorded in a high-
704 resolution, absolute-dated aragonite speleothem from eastern China. *Earth and*
705 *Planetary Science Letters*, *275*, 296-307.

706 Hodge, E. J., Richards, D. A., Smart, P. L., Andreo, B., Hoffmann, D. L.,
707 Matthey, D. P. & Gonzalez-Ramsan, A. (2008) Effective precipitation in southern
708 Spain (266 to 46ka) based on a speleothem stable carbon isotope record.
709 *Quaternary Research*, *69*, 447-457.

710 Cosford, J., Qing, H., Matthey, D., Eglington, B. & Zhang, M. (2009) Climatic
711 and local effects on stalagmite $\delta^{13}\text{C}$ values at Lianhua Cave, China.
712 *Palaeogeography, Palaeoclimatology, Palaeoecology*, *280*, 235-244.

713 Cosford, J., Qing, H., Lin, Y., Eglinton, B., Matthey, D., Chen, Y.G., Zhang, M.
714 and Cheng, H. (2010) The East Asian monsoon during MIS 2 expressed in a
715 speleothem $\delta^{18}\text{O}$ record from Jintanwan Cave, Hunan, China. *Quaternary Research*,
716 73, 541-549.

717 Baker, A., Wilson, R., Fairchild, I. J., Franke, J., Spötl, C., Matthey, D., Trouet,
718 V. & Fuller, L. (2011) High resolution $\delta^{18}\text{O}$ and $\delta^{13}\text{C}$ records from an annually
719 laminated Scottish stalagmite and relationship with last millennium climate. *Global
720 and Planetary Change*, 79, 303-311.

721 Baldini, L. M., McDermott, F., Baldini, J. U. L., Arias, P., Cueto, M., Fairchild, I.
722 J., Hoffmann, D. L., Matthey, D. P., Müller, W., Nita, D. C., Ontañón, R., García-
723 Moncó, C. & Richards, D. A. (2015) Regional temperature, atmospheric circulation,
724 and sea-ice variability within the Younger Dryas Event constrained using a
725 speleothem from northern Iberia. *Earth and Planetary Science Letters*, 419, 101-110.

726 Othman, H., San Roman Alerigi, D., Batarseh, S., & Al Obaid, O. (2019,
727 November). Efficiency of High Power Laser in Carbonate Formations. In *Abu Dhabi
728 International Petroleum Exhibition & Conference*. Society of Petroleum Engineers.

729 Turchetta, S., & Carrino, L. (2005). An energy based model for laser cutting
730 natural stone. *International Journal of Machine Tools and Manufacture*, 45(7-8), 761-
731 767.

732 San-Roman-Alerigi, D. P., Han, Y., & Batarseh, S. I. (2017). Thermal and
733 geomechanical dynamics of high power electromagnetic heating of rocks. In *SPE
734 Middle East Oil & Gas Show and Conference*. Society of Petroleum Engineers.

735 San-Roman-Alerigi, D. P., van Dijk, C. P., Lube, V., & Lubineau, G. (2018).
736 Characterizing the Effects of High Power Laser Performance on Carbonate
737 Rocks. *Mineralogy and Geomechanical Analysis for Hydraulic Fracturing: An
738 Integrated Approach to Assess Rock Fracability in Sandstone Reservoirs see page 2
739 A Field Case Study of an Interwell Gas Tracer Test for Gas EOR Monitoring see
740 page 27, 47*.

741 Engler, P., Santana, M. W., Mittleman, M. L., & Balazs, D. (1989). Non-
742 isothermal, in situ XRD analysis of dolomite decomposition. *Thermochimica
743 Acta*, 140, 67-76.

744 Coplen, T. B., Brand, W. A., Gehre, M., Gröning, M., Meijer, H. A., Toman, B.,
745 & Verkouteren, R. M. (2006). New guidelines for $\delta^{13}\text{C}$ measurements. *Analytical
746 Chemistry*, 78(7), 2439-2441.

- 747 Böttcher, M. E. (1996). $^{18}\text{O}/^{16}\text{O}$ and $^{13}\text{C}/^{12}\text{C}$ fractionation during the reaction of
748 carbonates with phosphoric acid: effects of cationic substitution and reaction
749 temperature. *Isotopes in environmental and health studies*, 32(2-3), 299-305.
- 750 Rosenbaum, J., & Sheppard, S. M. F. (1986). An isotopic study of siderites,
751 dolomites and ankerites at high temperatures. *Geochimica et cosmochimica*
752 *acta*, 50(6), 1147-1150.
- 753 Sharma, T., & Clayton, R. N. (1965). Measurement of $\text{O}^{18}\text{O}^{16}$ ratios of total
754 oxygen of carbonates. *Geochimica et Cosmochimica Acta*, 29(12), 1347-1353.
- 755 Powell, M. D., & Kyser, T. K. (1991). Analysis of $\delta^{13}\text{C}$ and $\delta^{18}\text{O}$ in calcite,
756 dolomite, rhodochrosite and siderite using a laser extraction system. *Chemical*
757 *Geology*, 94(1), 55-66.